

Unveiling the Fine Structural Distortion of Atomically Thin $\text{Bi}_2\text{O}_2\text{Se}$ by Third-Harmonic Generation

Jing Liang, Teng Tu, Guanchu Chen, Yuanwei Sun, Ruixi Qiao, He Ma, Wentao Yu, Xu Zhou, Chaojie Ma, Peng Gao,* Hailin Peng,* Kaihui Liu,* and Dapeng Yu

Bismuth oxyselenide ($\text{Bi}_2\text{O}_2\text{Se}$), a new type of 2D material, has recently attracted increased attention due to its robust bandgap, stability under ambient conditions, and ultrahigh electron mobility. In such complex oxides, fine structural distortion tends to play a decisive role in determining the unique physical properties, such as the ferrotational order, ferroelectricity, and magnetoelasticity. Therefore, an in-depth investigation of the fine structural symmetry of $\text{Bi}_2\text{O}_2\text{Se}$ is necessary to exploit its potential applications. However, conventional techniques are either time consuming or requiring tedious sample treatment. Herein, a noninvasive and high-throughput approach is reported for characterizing the fine structural distortion in 2D centrosymmetric $\text{Bi}_2\text{O}_2\text{Se}$ by polarization-dependent third-harmonic generation (THG). Unprecedentedly, the divergence between the experimental results and the theoretical prediction of the perpendicular component of polarization-dependent THG indicates a fine structural distortion, namely, a $<1.4^\circ$ rotation of the oxygen square in the tetragonal (Bi_2O_2) layers. This rotation breaks the intrinsic mirror symmetry of 2D $\text{Bi}_2\text{O}_2\text{Se}$, eventually reducing the symmetry from the D_{4h} to the C_{4h} point group. The results demonstrate that THG is highly sensitive to even fine symmetry variations, thereby showing its potential to uncover hidden phase transitions and interacting polarized sublattices in novel 2D material systems.

In crystalline solids, symmetry plays a fundamental role in determining the optical, mechanical, electrical, and magnetic properties of the material. The expanding family of 2D materials consists of various structures that provide new opportunities for an incredible variety of physical phenomena and the resulting

multifunctional applications.^[1–8] For example, the broken inversion symmetry in monolayer molybdenum disulfide (MoS_2) exhibits an easily accessible electronic valley degree of freedom, allowing for potential valleytronic device applications.^[9–11] In addition, due to the atomically layered structure, the stacking symmetry permits a new freedom to tailor the material properties. More specifically, noncentrosymmetric Bernal-stacked ABA trilayer graphene is a semimetal with a gate-tunable band overlap, while centrosymmetric ABC trilayer graphene is a semiconductor with an electrically tunable bandgap.^[12] Furthermore, the ultraflexibility of 2D materials makes it possible to reversibly modulate their physical properties, such as phase transitions and the related electrical properties, by applying strain. For example, it was reported that the $2\text{H}-1\text{T}'$ (semiconductor-semimetal) phase transition of molybdenum ditelluride (MoTe_2) was possible at room temperature under tensile strain.^[13–15] Intrinsic symmetry characterization is therefore

necessary to gain a better understanding of the interesting properties of 2D materials and promote their future scientific and industrial applications.

In addition to standard crystallographic symmetry, fine structural distortion is especially important in complex oxides,

J. Liang, G. C. Chen, H. Ma, Dr. W. T. Yu, Dr. X. Zhou, Dr. C. J. Ma, Prof. K. H. Liu
State Key Laboratory for Mesoscopic Physics
Frontiers Science Center for Nano-optoelectronics
School of Physics
Peking University
Beijing 100871, China
E-mail: khliu@pku.edu.cn

J. Liang, H. Ma, Prof. K. H. Liu
Academy for Advanced Interdisciplinary Studies
Collaborative Innovation Center of Quantum Matter
Peking University
Beijing 100871, China

T. Tu, G. C. Chen, Prof. H. L. Peng
Center for Nanochemistry
Beijing Science and Engineering Centre for Nanocarbons
College of Chemistry and Molecular Engineering
Peking University
Beijing 100871, China
E-mail: hlpeng@pku.edu.cn

Y. W. Sun, Dr. R. X. Qiao, Prof. P. Gao
International Center for Quantum Materials
Electron Microscopy Laboratory
School of Physics
Peking University
Beijing 100871, China
E-mail: p-gao@pku.edu.cn

Prof. D. P. Yu
Shenzhen Institute for Quantum Science and Engineering
and Department of Physics
Southern University of Science and Technology
Shenzhen 518055, China

 The ORCID identification number(s) for the author(s) of this article can be found under <https://doi.org/10.1002/adma.202002831>.

DOI: 10.1002/adma.202002831

as this tends to result in interesting ferroelectric properties, a giant photovoltaic effect, and magnetoelasticity.^[16–23] Recently, bismuth oxyselenide ($\text{Bi}_2\text{O}_2\text{Se}$), a new type of 2D material, has emerged as a promising alternative for next-generation electronic and optoelectronic applications owing to its robust bandgap, stability under ambient conditions, and ultrahigh electron mobility.^[24–27] In contrast to the well-known honeycomb-lattice 2D materials mentioned above that exhibit van der Waals interlayer coupling, 2D $\text{Bi}_2\text{O}_2\text{Se}$ consists of tetragonal Bi_2O_2 layers sandwiched between Se atomic sheets with weak interlayer electrostatic interactions. To understand the nature of the outstanding performance of 2D $\text{Bi}_2\text{O}_2\text{Se}$, an in-depth characterization of its crystallographic symmetry and possible fine structural distortion is crucial.

Conventional techniques, including transmission electron microscopy (TEM) and X-ray diffraction (XRD), can reveal important aspects of the symmetry properties, but they are often time consuming and require extensive sample preparation.^[28–30] Since the nonlinear optical susceptibility tensor encodes the symmetry information of a crystalline material, noninvasive and high-throughput nonlinear spectroscopy has been widely used to detect symmetry-related physical phenomena, including crystallographic orientations, phase transitions, grain boundaries, stacking orders, strain tensors, and magnetic orders.^[31–38] For example, the lowest-order second harmonic generation (SHG) has received particular attention since the higher-order process tends to be weaker, and requires a higher pump intensity in bulk materials. However, in 2D materials, third and high harmonic generations (THG/HHG) have shown relatively high conversion efficiencies.^[39] Furthermore, THG, an odd-order nonlinear process, does not have a symmetry constraint, such as in the case of the

inversion-symmetry-forbidden SHG. Therefore, THG could be suitable for the characterization of symmetry-related properties in centrosymmetric 2D materials.

Thus, we herein report a systematic symmetry study of 2D centrosymmetric $\text{Bi}_2\text{O}_2\text{Se}$ based on the use of polarization-dependent THG. We observed a strong THG response of 2D $\text{Bi}_2\text{O}_2\text{Se}$, which indicates the feasibility for potential optical imaging and symmetry characterization. As expected, the parallel component of the polarization-dependent THG pattern exhibits a one-to-one correspondence with the lattice orientation. However, we observed that the perpendicular component of the polarization-dependent THG pattern has two sets of four equal petals, which differs significantly from the theoretically predicted eight equal petals. We demonstrate that this discrepancy stems from the fine structural distortion of 2D $\text{Bi}_2\text{O}_2\text{Se}$. More specifically, the rotation of an oxygen square in the tetragonal Bi_2O_2 layers breaks the mirror symmetry, and reduces the crystallographic symmetry from intrinsic D_{4h} to C_{4h} , ultimately resulting in a different THG pattern. Our results suggest that THG can be employed as a rapid and sensitive method to the characterize crystallographic symmetry of a material, and unveil fine structural distortions, which are necessary to produce unique physical phenomena in a wide range of material systems.

For symmetry characterization, we first investigated the third-order nonlinear optical response of $\text{Bi}_2\text{O}_2\text{Se}$. For this purpose, few-layer $\text{Bi}_2\text{O}_2\text{Se}$ nanoplates with a domain size up to $100\ \mu\text{m}$ were grown on a mica substrate using chemical vapor deposition (CVD) (Figure 1a and Experimental Section). The square morphology in the optical image indicates the tetragonal crystallographic symmetry (Figure 1b), which is consistent with previous reports.^[40] The characteristic out-of-plane vibration A_{1g}

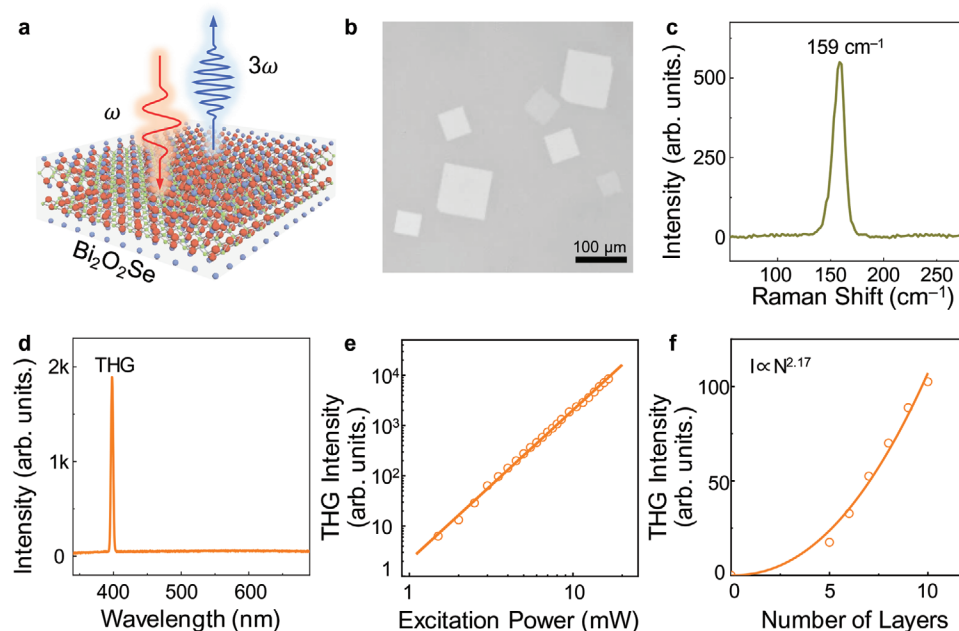


Figure 1. THG response of 2D $\text{Bi}_2\text{O}_2\text{Se}$. a) Schematic diagram of the THG process in $\text{Bi}_2\text{O}_2\text{Se}$ nanoplates. The left red and right blue waves indicate the excitation beam (ω) and the generated THG signal (3ω), respectively. b) Optical image of the $\text{Bi}_2\text{O}_2\text{Se}$ nanoplates of different thickness. c) Raman spectrum of the $\text{Bi}_2\text{O}_2\text{Se}$ nanoflakes. d) Nonlinear optical response of the $\text{Bi}_2\text{O}_2\text{Se}$ nanoflakes. The sharp peak centered at $400\ \text{nm}$ is the THG signal. e) Excitation power dependence of the THG signals of the $\text{Bi}_2\text{O}_2\text{Se}$ nanoflakes. f) THG intensity as a function of the layer number of $\text{Bi}_2\text{O}_2\text{Se}$ nanoplates.

mode of $\text{Bi}_2\text{O}_2\text{Se}$ was also observed at $\approx 159\text{ cm}^{-1}$ in the Raman spectrum (Figure 1c). Nonlinear optical harmonic generation is a process in which the frequency of the incident light ω is converted into higher harmonics $n\omega$ ($n = 2, 3, 4, \dots$) through its nonlinear interaction with a material. In our experiments, under the excitation of a normally incident linearly polarized pulse laser (1200 nm, 76 MHz), both SHG (600 nm, $n = 2$) and THG (400 nm, $n = 3$) signals generated from a nonlinear optical material were collected simultaneously (Figure 1a). As expected, the SHG signal from $\text{Bi}_2\text{O}_2\text{Se}$ diminished to almost zero due to the inversion symmetry of the D_{4h} crystallographic point group (Figure 1d). The sharp peak centered at 400 nm exhibited a cubic dependence on excitation power, further confirming the THG process (Figure 1e). Comparing the THG responses of 2D $\text{Bi}_2\text{O}_2\text{Se}$ and monolayer WS_2 , 2D $\text{Bi}_2\text{O}_2\text{Se}$ was confirmed to possess a large third-order nonlinear susceptibility (Figures S1 and S2, Supporting Information).

The strong THG response suggested that imaging of $\text{Bi}_2\text{O}_2\text{Se}$ by THG spectroscopy may be possible. Thus, the dependence of the THG intensity on the number of layers (N) was investigated. As expected, the THG intensity exhibited a perfectly quadratic increase with increasing N , since the THG intensity was mainly determined by the thickness of the 2D $\text{Bi}_2\text{O}_2\text{Se}$ (Figure 1f); depletion of the excitation light and the phase mismatch were negligible due to the atomic thickness.^[37] According to our experimental results, THG has the potential to sensitively identify N up to at least 10. Therefore, THG images for $\text{Bi}_2\text{O}_2\text{Se}$ nanoplates with the same orientation but with different thickness ($N = 6, 7$) were obtained by scanning the sample stage (Figure 2a,c and Figure S3, Supporting Information). Instead of linear absorption, the THG image (Figure 2b) showed a higher contrast than that of the optical image (Figure 2a). Due to the advantages of a strong THG response and the high-sensitivity of the thickness-dependent process, THG may be suitable for rapid and sensitive optical imaging of such materials.

We also performed a preliminary study of the symmetry sensitivity of THG. In this context, we note that the grain boundary is the interface between the domains of a material with different crystallographic orientations. If the THG signal is sensitive to the crystallographic orientation of $\text{Bi}_2\text{O}_2\text{Se}$, a clear contrast between the different domains should be observable by mapping the THG intensity with the emission field polarization parallel to the excitation field. Figure 2d shows a typical optical image of a $\text{Bi}_2\text{O}_2\text{Se}$ flake with an irregular shape. Although the sample appears uniform in the optical image, THG mapping of the same area reveals that the sample is stitched together from two individual domains, between which is a sharp boundary (Figure 2e). The contrast between the various domains is due to the anisotropic THG response of $\text{Bi}_2\text{O}_2\text{Se}$ (Figure 2f). THG is clearly sensitive to the crystallographic orientation, thereby providing tremendous opportunities for its use in symmetry-related characterization.

To determine the relationship between THG and the crystallographic symmetry of $\text{Bi}_2\text{O}_2\text{Se}$, polarization-dependent THG measurements are necessary (Figure 3). We note that previous studies have assigned $\text{Bi}_2\text{O}_2\text{Se}$ to the centrosymmetric tetragonal D_{4h} crystallographic point group.^[24] Due to the 2D nature of the $\text{Bi}_2\text{O}_2\text{Se}$ nanoplates and the normal incidence in our configuration, all components in the third-order nonlinear susceptibility $\chi_{\text{int}}^{(3)}$ that contain an out-of-plane c term were set to zero, since they do not contribute to the final THG response. Therefore, only eight nonzero elements remained in the $\chi_{\text{int}}^{(3)}$ tensor

$$\chi_{\text{int}}^{(3)} = \begin{pmatrix} \chi_{aaaa} & 0 & 0 & 0 & \chi_{aabb} & \chi_{abab} & \chi_{abba} & 0 \\ 0 & \chi_{baab} & \chi_{baba} & \chi_{bbaa} & 0 & 0 & 0 & \chi_{bbbb} \end{pmatrix} \quad (1)$$

where a and b are the in-plane orthogonal crystal coordinates along the B–O bonding directions (Figure 3a). The final intensity of the THG signal can therefore be expressed as

$$I_{\text{THG}} = |\hat{e}_{3\omega} \chi_{\text{int}}^{(3)} \hat{e}_{\omega}^3|^2 \quad (2)$$

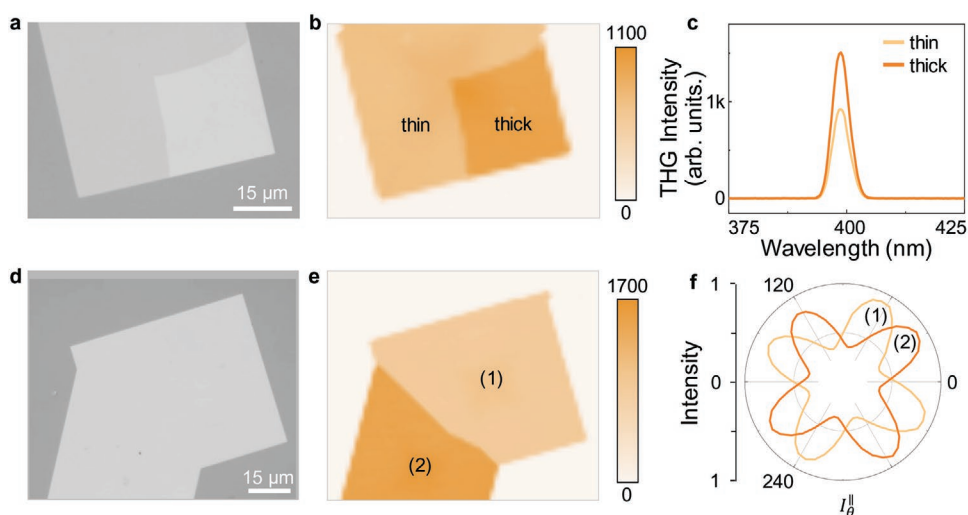


Figure 2. Thickness imaging and boundary visualization of 2D $\text{Bi}_2\text{O}_2\text{Se}$ by THG. a) Optical image of a $\text{Bi}_2\text{O}_2\text{Se}$ nanoplate with different thicknesses (6L/7L). b) THG image of the $\text{Bi}_2\text{O}_2\text{Se}$ nanoplate shown in (a). c) THG spectra of the $\text{Bi}_2\text{O}_2\text{Se}$ nanoplate shown in (b). d) Optical image of a polycrystalline $\text{Bi}_2\text{O}_2\text{Se}$ nanoplate consisting of two individual grains. e) THG image of the polycrystalline $\text{Bi}_2\text{O}_2\text{Se}$ nanoplate shown in (d). The boundary between domains (1) and (2) can be clearly visualized. f) θ -Dependent parallel component I_{θ}^{\parallel} of THG from different grains of the $\text{Bi}_2\text{O}_2\text{Se}$ nanoplate shown in (e).

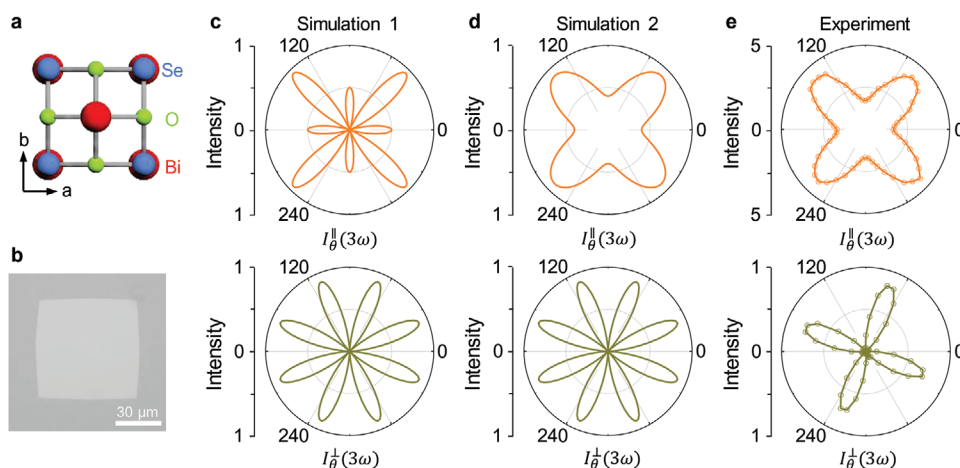


Figure 3. Polarization-dependent THG patterns of the $\text{Bi}_2\text{O}_2\text{Se}$ nanoplates. a) Top view of the crystal structure of $\text{Bi}_2\text{O}_2\text{Se}$ observed using a ball-stick model. b) Optical image of 5L $\text{Bi}_2\text{O}_2\text{Se}$. c,d) The simulated θ -dependent parallel I_{θ}^{\parallel} and perpendicular I_{θ}^{\perp} component of THG from D_{4h} $\text{Bi}_2\text{O}_2\text{Se}$ when c) $B < -3A$ or d) $B > A$. θ is the incident laser polarization from the horizontal direction. e) Experimental results of the θ -dependent parallel I_{θ}^{\parallel} and perpendicular I_{θ}^{\perp} component of THG from the $\text{Bi}_2\text{O}_2\text{Se}$ nanoplate shown in (b).

where $\hat{e}_{\omega} = (\cos \theta \quad \sin \theta)$ is the unit polarization vector of the incident light ω , and θ is the incident light polarization angle relative to the a -axis. When the polarization of the THG signal $\hat{e}_{3\omega} = (\cos \theta \quad \sin \theta)$ ($\hat{e}_{3\omega} = (-\sin \theta \quad \cos \theta)$) is parallel (perpendicular) to the excitation polarization, the parallel (perpendicular) component of the polarization-dependent THG can be obtained

$$I_{\text{int}}^{\parallel} = \left| A - \frac{1}{4}(A - B)(1 - \cos 4\theta) \right|^2$$

$$I_{\text{int}}^{\perp} = \left| \frac{1}{4}(A - B) \sin 4\theta \right|^2 \quad (3)$$

where $A = \chi_{aaaa} = \chi_{bbbb}$ and $B = \chi_{aabb} + \chi_{abab} + \chi_{abba} = \chi_{bbba} + \chi_{baba} + \chi_{baab}$ ($A \neq B$) are the only two independent variables. According to the relationship between A and B , the parallel component $I_{\text{int}}^{\parallel}$ may contain six kinds of patterns with either four or eight petals, while the perpendicular component I_{int}^{\perp} always exhibits the same eight-fold rotational symmetric pattern (Figure 3c,d, and Figure S4, Supporting Information). This is determined by the four-fold rotation symmetry and the mirror symmetries about the ac , bc , or diagonal planes of the D_{4h} crystallographic point group.

We further probed the crystallographic symmetry of $\text{Bi}_2\text{O}_2\text{Se}$ by polarization-dependent THG measurements (Figure 3b), which showed that the parallel component of the polarization-dependent THG pattern I^{\parallel} had a clear four-petal pattern. This pattern is comparable to that shown in Figure 3d, where the peak of each petal is parallel to the diagonal direction of the in-plane Bi–O direction. This indicates that the square shape of $\text{Bi}_2\text{O}_2\text{Se}$ has a one-to-one correspondence with the lattice symmetry, and that the CVD-grown $\text{Bi}_2\text{O}_2\text{Se}$ nanoplates possess Bi–O edge configurations. This observation is consistent with the structural morphology reported previously.^[24]

However, the perpendicular component of the polarization-dependent THG I^{\perp} differed significantly from the theoretical prediction, in that it has eight petals of alternating magnitudes, and the single set of four petals almost completely disappeared (Figure 3e). A similar result was observed when the analyzer

and polarizer were not perfectly perpendicular (Note S1, Supporting Information). This instrumental error was successfully ruled out by detecting the polarization-dependent THG pattern under a series of relative angles from -8° to 8° (Figure S5, Supporting Information). We also excluded a wide range of possible interpretations of the substrate effect, a specific electronic state resonance, and light-induced phase transition through the use of samples suspended on a porous carbon membrane supported by a copper grid, in addition to different incident wavelengths, and different excitation powers, respectively (Figures S6–S8, Supporting Information). Hence, we finally concluded that the discrepancy originates from the crystallographic symmetry reduction of $\text{Bi}_2\text{O}_2\text{Se}$. Both the experimental I^{\parallel} and I^{\perp} patterns were best described by the C_{4h} crystallographic point group

$$I_{\text{exp}}^{\parallel} = \left| A - \frac{1}{4}(A - B)(1 - \cos 4\theta) \right|^2$$

$$I_{\text{exp}}^{\perp} = \left| \frac{1}{4}(A - B) \sin 4\theta + D - \frac{1}{4}(D - C)(1 - \cos 4\theta) \right|^2 \quad (4)$$

where A and B have the same form as in Equation (3). Here, $C = \chi_{abaa} + \chi_{aaba} + \chi_{aaab} = \chi_{babb} + \chi_{bbab} + \chi_{bbba}$ and $D = \chi_{abbb} = \chi_{baaa}$ ($C \neq D$) are two new independent variables. This implies that the four-fold rotation symmetry is reserved, but the mirror symmetries are actually absent. In each layer, compared with the standard crystal structure of 2D $\text{Bi}_2\text{O}_2\text{Se}$ (Figure 4a), the most likely hypothesis is that the oxygen square in the Bi_2O_2 layers undergoes a staggered counterclockwise and clockwise rotation, which finally breaks the mirror symmetries (Figure 4b). In addition, it is likely that in a few layers, different stacking orders of the two equivalent patterns of oxygen square rotation shown in Figure 4b could lead to different crystallographic symmetries. When two equivalent patterns are stacked, 2D $\text{Bi}_2\text{O}_2\text{Se}$ belongs to the D_4 crystallographic point group (Figure 4c). In this case, although mirror symmetries about the ac or bc planes are absent, the two-fold axes along the a - or b -axes remain. Hence, the polarization-dependent THG pattern should have

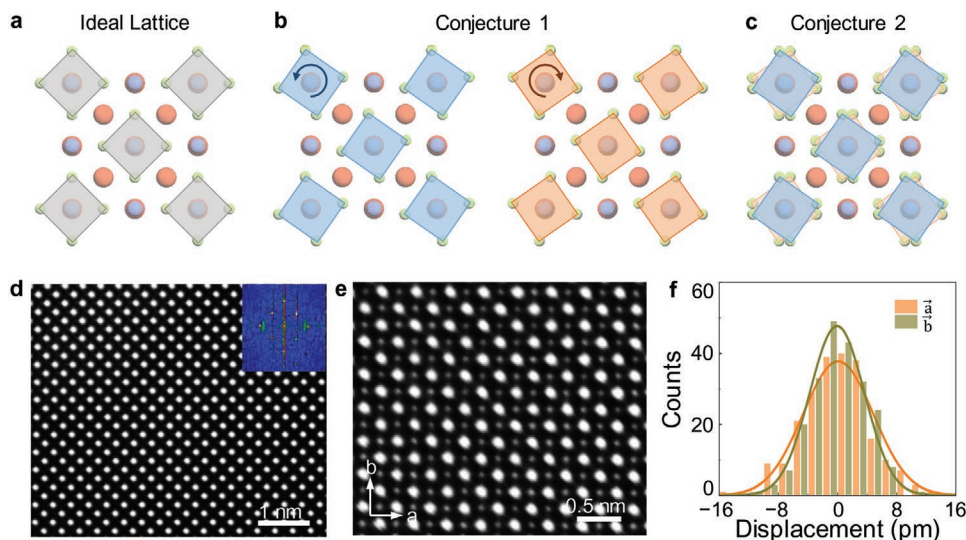


Figure 4. Possible $\text{Bi}_2\text{O}_2\text{Se}$ lattice structure and TEM characterization. a) Top view of the ideal tetragonal lattice of D_{4h} $\text{Bi}_2\text{O}_2\text{Se}$. b, c) Possible structural distortion in $\text{Bi}_2\text{O}_2\text{Se}$. d) Atomically resolved HAADF image with the FFT pattern shown in the inset. e) iDPC image from the selected region in (d). f) Statistics histogram of the O atom displacement distribution along the a and b axes as shown in (e).

the same pattern as the intrinsic D_{4h} crystallographic point group. Therefore, only homogeneous stacking is allowed, and the formed $\text{Bi}_2\text{O}_2\text{Se}$ belongs to the C_{4h} crystallographic point group, which is consistent with the theoretical analysis.

Experimentally, scanning transmission electron microscopy (STEM) using a high-angle annular dark field (HAADF) detector provides an atomically planar view of $\text{Bi}_2\text{O}_2\text{Se}$ (Figure 4d), and the fast Fourier transform (FFT) image shows only a single set of diffraction patterns. This confirms that the described reduction in the crystallographic symmetry is a result of fine structural distortion of each layer, instead of twisted stacking between adjacent ideal-lattice layers (inset of Figure 4d). To visualize the rotation of O atoms, we used integrated differential phase contrast imaging (iDPC) to extract the precise atomic shifts based on the anion sublattice with respect to the cations (Figure 4e). In principle, two typical peaks with equal magnitudes and opposite signs should be observed in the distribution histogram of the O atomic shift along both the *a*-axis and the *b*-axis. However, the distribution histogram shows no observable atomic displacement of the O atom along either axis (Figure 4f). Calculations assuming a root-mean-square value of ≈ 4.8 pm gave a rotation angle of the oxygen square of $<1.4^\circ$. We therefore concluded that THG is able to unveil fine structural distortion in 2D materials, especially when attributed to crystallographic symmetry evolution.

It is well-known that symmetry has a critical effect on the physical properties of crystalline materials, where even small crystallographic distortions can have huge ramifications. A typical example is oxygen octahedral distortions in perovskite compounds, including tilts, rotations, deformations, and off-centering, which provide a broad scope for various functional phenomena, such as high T_c superconductivity, ferroelectricity, magnetoelasticity, and the giant photovoltaic effect.^[16–23] SHG, the lowest-order nonlinear optical process, has been the focus for investigating such unique phenomena because of its sensitivity to both the spatial-inversion and time-reversal

symmetry. For example, SHG has been used to reveal the tetragonal distortions of O octahedra-induced magnetoelastic locking in Sr_2IrO_4 ,^[41] spin rotation-induced ferrotoroidic order in LiCoPO_4 ,^[42] and O octahedra rotation-induced ferrorotational order in $\text{RbFe}(\text{MnO}_4)_2$.^[43] However, one key restriction is that SHG is only permitted in noncentrosymmetric crystalline materials.

In this work, we systematically studied the intrinsic symmetry and demonstrated the fine structural distortion in centrosymmetric $\text{Bi}_2\text{O}_2\text{Se}$ using THG, which is the universal third-order nonlinear optical process. The 2D $\text{Bi}_2\text{O}_2\text{Se}$ nanoplates gave a strong THG response, which is a prerequisite for various symmetry-related applications. Our results indicated that the crystallographic orientation of $\text{Bi}_2\text{O}_2\text{Se}$ can easily be determined through the parallel component of the polarization-dependent THG pattern. Moreover, based on experimental verification and theoretical analysis, we showed that the broken mirror symmetry in the perpendicular component of the polarization-dependent THG pattern directly indicates underlying fine structural distortion, namely a small oxygen square rotation in the Bi_2O_2 layers. THG characterization of fine structure distortion in centrosymmetric materials therefore compensates for the symmetry limitation of SHG. In conjunction with SHG, THG analyses could promote the development of novel crystallographic or magnetic structures with unique physical phenomena. In the near future, we will focus on expanding the application of nonlinear optical methods for characterizing 2D materials and exploring the potential physical properties due to such fine structural distortion in 2D $\text{Bi}_2\text{O}_2\text{Se}$.

Experimental Section

CVD Growth and Characterization of $\text{Bi}_2\text{O}_2\text{Se}$ Nanoplates: 2D $\text{Bi}_2\text{O}_2\text{Se}$ crystals were synthesized according to a previously reported procedure

inside a home-made low-pressure CVD system.^[24] More specifically, Bi₂O₃ powder (Alfa Aesar, USA, 5 N) and Bi₂Se₃ pieces (Alfa Aesar, USA, 5 N) were placed in the hot zone center and upstream area of a horizontal tube furnace, respectively. High-purity argon gas was used as the carrier gas to transport the vapor precursor to the downstream region, which lay at a distance of ≈8–12 cm from the center. Freshly cleaved fluorophlogopite mica was placed in the downstream area as the growth substrate. Typical growth conditions were as follows: source temperature =600–620 °C, growth substrate temperature =480–550 °C, system pressure =100–400 Torr, carrier gas =160–230 sccm argon mixed with a trace amount of oxygen, and growth time =5–30 min. The as-grown Bi₂O₂Se nanoplates were then examined by optical microscopy (Olympus BX51) and atomic force microscopy (AFM, Bruker Dimension Icon with a Nanoscope V controller). Atomically resolved HAADF and iDPC images were recorded using an aberration-corrected FEI Titan Cube Themis G2 system operating at 300 kV. Prior to characterization, the samples were transferred onto a porous carbon film supported by a copper grid using a polymethyl methacrylate assisted transfer method, with a dilute HF solution (5%) being used as the substrate etching reagent.

Experimental THG Setup: Micrographs of the WS₂ flakes on the flexible substrate acrylic were recorded using an Olympus microscope (Olympus BX51). The PL and Raman spectra were recorded using a home-built confocal microscopy system with a laser excitation wavelength of 532 nm and an average power of 200 μW. Femtosecond pulses (≈100 fs, 76 MHz) at 1200 nm were generated by a Ti:sapphire oscillator (Coherent Mira-HP) equipped with an optical parametric oscillator (Coherent Mira-OPO-X). The excitation beam was normally incident, and its linear polarization was controlled by a half-wave plate in front of the objective (40×, N.A. = 0.65). In the reflection geometry, a linear analyzer parallel (perpendicular) to the incident polarization was used to extract the parallel (perpendicular) component I_{\parallel} (I_{\perp}) of THG from the sample. The signal was recorded using a grating spectrograph with a charge-coupled device camera (Princeton SP-2500i).

Supporting Information

Supporting Information is available from the Wiley Online Library or from the author.

Acknowledgements

J.L. and T.T. contributed equally to this work. This work was supported by The Key R&D Program of Guangdong Province (2019B010931001, 2020B010189001, 2018B010109009, and 2018B030327001), the National Natural Science Foundation of China (51991340, 51991342, 21920102004, 21733001, 21525310, and 51672007), Beijing Natural Science Foundation (JQ19004), Beijing Excellent Talents Training Support (2017000026833ZK11), the National Key R&D Program of China (2016YFA0300903 and 2016YFA0300804), the Beijing Municipal Science & Technology Commission (Z191100007219005), the Beijing Graphene Innovation Program (Z181100004818003), the Bureau of Industry and Information Technology of Shenzhen (Graphene platform 201901161512), the Guangdong Innovative and Entrepreneurial Research Team Program (2016ZT06D348), the Science, Technology and Innovation Commission of Shenzhen Municipality (KYTDPT20181011104202253), the National Equipment Program of China (ZDYZ2015-1), and the China Postdoctoral Science Foundation (2019M660281).

Conflict of Interest

The authors declare no conflict of interest.

Keywords

2D materials, fine structural distortion, third-harmonic generation

Received: April 26, 2020

Revised: May 21, 2020

Published online:

- [1] L. T. Dou, A. B. Wong, Y. Yu, M. L. Lai, N. Kornienko, *Science* **2015**, 349, 1518.
- [2] J. R. Schaibley, H. Y. Yu, G. Clark, P. Rivera, J. S. Ross, *Nat. Rev. Mater.* **2016**, 1, 16055.
- [3] C. Z. Ning, L. T. Dou, P. D. Yang, *Nat. Rev. Mater.* **2017**, 2, 17070.
- [4] C. J. Cui, F. Xue, W. J. Hu, L. J. Li, *npj 2D Mater. Appl.* **2018**, 2, 18.
- [5] T. Mueller, E. Malic, *npj 2D Mater. Appl.* **2018**, 2, 29.
- [6] Y. Liu, M. Siron, D. L. Lu, J. J. Yang, R. dos Reis, *J. Am. Chem. Soc.* **2019**, 141, 13028.
- [7] K. F. Mak, J. Shan, D. C. Ralph, *Nat. Rev. Phys.* **2019**, 1, 646.
- [8] Z. H. Wu, J. H. Hao, *npj 2D Mater. Appl.* **2020**, 4, 4.
- [9] T. Cao, G. Wang, W. P. Han, H. Q. Ye, C. R. Zhu, *Nat. Commun.* **2012**, 3, 887.
- [10] K. F. Mak, K. L. He, J. Shan, T. F. Heinz, *Nat. Nanotechnol.* **2012**, 7, 494.
- [11] H. L. Zeng, J. F. Dai, W. Yao, D. Xiao, X. D. Cui, *Nat. Nanotechnol.* **2012**, 7, 490.
- [12] Y. W. Shan, Y. G. Li, D. Huang, Q. J. Tong, W. Yao, *Sci. Adv.* **2018**, 4, eaat0074.
- [13] S. Cho, S. Kim, J. H. Kim, J. Zhao, J. Seok, *Science* **2015**, 349, 625.
- [14] R. Beams, L. G. Cancado, S. Krylyuk, I. Kalish, B. Kalanyan, *ACS Nano* **2016**, 10, 9626.
- [15] S. Song, D. H. Keum, S. Cho, D. Perello, Y. Kim, *Nano Lett.* **2016**, 16, 188.
- [16] A. Vonhippel, *Rev. Mod. Phys.* **1950**, 22, 221.
- [17] J. G. Bednorz, K. A. Muller, *Rev. Mod. Phys.* **1988**, 60, 585.
- [18] M. Uehara, S. Mori, C. H. Chen, S. W. Cheong, *Nature* **1999**, 399, 560.
- [19] M. B. Salamon, M. Jaime, *Rev. Mod. Phys.* **2001**, 73, 583.
- [20] S. W. Cheong, M. Mostovoy, *Nat. Mater.* **2007**, 6, 13.
- [21] T. Choi, S. Lee, Y. J. Choi, V. Kiryukhin, S. W. Cheong, *Science* **2009**, 324, 63.
- [22] M. Lilienblum, T. Lottermoser, S. Manz, S. M. Selbach, A. Cano, *Nat. Phys.* **2015**, 11, 1070.
- [23] T. F. Nova, A. S. Disa, M. Fechner, A. Cavalleri, *Science* **2019**, 364, 1075.
- [24] J. X. Wu, H. T. Yuan, M. M. Meng, C. Chen, Y. Sun, *Nat. Nanotechnol.* **2017**, 12, 530.
- [25] J. B. Yin, Z. J. Tan, H. Hong, J. X. Wu, H. T. Yuan, *Nat. Commun.* **2018**, 9, 3311.
- [26] C. Chen, M. X. Wang, J. X. Wu, H. X. Fu, H. F. Yang, *Sci. Adv.* **2018**, 4, eaat8355.
- [27] Y. Liang, Y. J. Chen, Y. W. Sun, S. P. Xu, J. X. Wu, *Adv. Mater.* **2019**, 31, 1901964.
- [28] G. S. Armatas, M. G. Kanatzidis, *Nature* **2006**, 441, 1122.
- [29] A. M. van der Zande, P. Y. Huang, D. A. Chenet, T. C. Berkelbach, Y. M. You, *Nat. Mater.* **2013**, 12, 554.
- [30] S. Najmaei, Z. Liu, W. Zhou, X. L. Zou, G. Shi, *Nat. Mater.* **2013**, 12, 754.
- [31] X. B. Yin, Z. L. Ye, D. A. Chenet, Y. Ye, K. O'Brien, *Science* **2014**, 344, 488.
- [32] W. T. Hsu, Z. A. Zhao, L. J. Li, C. H. Chen, M. H. Chiu, *ACS Nano* **2014**, 8, 2951.
- [33] J. X. Cheng, T. Jiang, Q. Q. Ji, Y. Zhang, Z. M. Li, *Adv. Mater.* **2015**, 27, 4069.

- [34] J. Liang, J. Zhang, Z. Z. Li, H. Hong, J. H. Wang, *Nano Lett.* **2017**, *17*, 7539.
- [35] L. Karvonen, A. Saynatjoki, M. J. Huttunen, A. Autere, B. Amirsolaimani, *Nat. Commun.* **2017**, *8*, 15714.
- [36] E. J. Sie, C. M. Nyby, C. D. Pemmaraju, S. J. Park, X. Z. Shen, *Nature* **2019**, 565, 61.
- [37] J. Liang, J. H. Wang, Z. H. Zhang, Y. Z. Su, Y. Guo, *Adv. Mater.* **2019**, *31*, 1808160.
- [38] Z. Y. Sun, Y. F. Yi, T. C. Song, G. Clark, B. Huang, *Nature* **2019**, 572, 497.
- [39] A. Saynatjoki, L. Karvonen, H. Rostami, A. Autere, S. Mehravar, *Nat. Commun.* **2017**, *8*, 893.
- [40] J. X. Wu, C. W. Tan, Z. J. Tan, Y. J. Liu, J. B. Yin, *Nano Lett.* **2017**, *17*, 3021.
- [41] D. H. Torchinsky, H. Chu, L. Zhao, N. B. Perkins, Y. Sizyuk, *Phys. Rev. Lett.* **2015**, *114*, 096404.
- [42] B. B. Van Aken, J. P. Rivera, H. Schmid, M. Fiebig, *Nature* **2007**, 449, 702.
- [43] W. C. Jin, E. Drueke, S. W. Li, A. Admasu, R. Owen, *Nat. Phys.* **2020**, *16*, 42.